ResearchGate

See discussions, stats, and author profiles for this publication at: https://www.researchgate.net/publication/340582495

LiQi-2020-GJI_Two main rupture stages during the 2018 magnitude 7.5 Sulawesi earthquake

Article *in* Geophysical Journal International · March 2020

DOI: 10.1093/gji/ggaa115

CITATIONS
0

READS
94

4 authors, including:

Qi Li
Institute of Seismology, China Earthquake Administration
8 PUBLICATIONS **14** CITATIONS

SEE PROFILE

Bin Zhao
Institute of Seismology, China Earthquake Administration
32 PUBLICATIONS **294** CITATIONS

SEE PROFILE

Wenbin Xu
Central South University
49 PUBLICATIONS **420** CITATIONS

SEE PROFILE

Some of the authors of this publication are also working on these related projects:

Project Crustal deformation monitoring by geodesy View project

Project Crustal deformation monitoring by geodesy View project

All content following this page was uploaded by Qi Li on 12 April 2020.

The user has requested enhancement of the downloaded file.

Geophysical Journal International

Geophys. J. Int. (2020) Volume **221**, Issue 3**, Pages 1873-1882** GJI Seismology

doi: 10.1093/gji/ggaa115

Two main rupture stages during the 2018 magnitude 7.5 Sulawesi earthquake

Qi Li,[1] Bin Zhao,[1] Kai Tan[1] and Wenbin Xu[2]

[1]*Key Laboratory of Earthquake Geodesy, Institute of Seismology, China Earthquake Administration, Wuhan, China. Email:* whgpstan@163.com
[2]*Department of Land Surveying and Geo-informatics, The Hong Kong Polytechnic University, Hong Kong, China*

Received 2020 March 4; in original form 2019 May 29

SUMMARY

On 28 September 2018, a M_w 7.5 strike-slip earthquake occurred in Sulawesi Island, Indonesia, and it unexpectedly triggered a tsunami. To clearly understand the spatiotemporal evolution process of source rupture, we collected the far-field body wave data and utilized the back-projection method together with finite fault inversion method to investigate the rupture kinematics of this earthquake. Results obtained with the two methods have good consistency and complementarity. We hold that the rupture expanded from the epicentre and propagated bilaterally towards the north and south along the strike direction during the first 24 s, and then to the south. Therefore, the whole rupture process consists of two main stages. For the second stage, the fault segment experienced most of the moment release between 0 and 15 km depth, while the fault plane tended to slip at greater depth (down to 20 km) in the first stage. The total length of the rupture was about 200 km and the seismic moment was $\sim 2.48 \times 10^{20}$ Nm, which was equivalent to M_w 7.5. The surface rupture was evident and the maximum slip of 6.24 m was observed in the Palu basin, which was close to Palu city. The rupture was dominated by left-lateral strike-slip with both normal and thrust components as well. The normal slip exhibited in the shallow part of the fault on the north side of Palu bay together with the special geographical location of Palu bay likely favored tsunami genesis.

Key words: Inverse theory; Earthquake dynamics; Body waves; Wave propagation; Earthquake source observations.

1 INTRODUCTION

On 28 September 2018, a M_w 7.5 earthquake struck Sulawesi Island, Indonesia, triggering a tsunami (Mai 2019). Its shaking, for its magnitude, seemed especially powerful, causing widespread soil liquefaction and landslides (Socquet *et al.* 2019). The earthquake and tsunami killed more than 2000 people and forced tens of thousands of people to evacuate their homes (Mai 2019). The city of Palu, about 75 km from the epicentre of the earthquake, was seriously affected. According to the determination results of the United States Geological Survey (USGS, https://www.usgs.gov/natural-hazards/earthquake-hazards/earthquakes), the epicentre of the earthquake was 0.256°S, 119.846°E, and the focal depth was 20 ± 1.8 km. The focal mechanism solution determined by the Global Centroid-Moment-Tensor (GCMT, https://www.globalcmt.org/) shows that the seismogenic fault has a strike of 348°, a dip angle of 57° and a slip angle of –15°, so the rupture is a rupture event dominated by sinistral strike-slip and having normal fault characteristic.

The Palu earthquake occurred at the junction of the Australian, Sunda and Philippine plates, with strong tectonic activity in the focal area (Fig. 1a, Puntodewo *et al.* 1994; Rangin *et al.* 1999; Socquet *et al.* 2006). Sulawesi Island, Indonesia has very complex geological conditions and it is a natural disaster-prone area with such natural disasters as earthquake, volcanic eruption and tsunami (Vigny *et al.* 2002; Watkinson & Hall 2016). In the past near 100 yr since 1927, the area has been hit by six tsunamis, including two ones occurring in the Palu Bay (Prasetya *et al.* 2001). The basin where the city of Palu is located is a nearly N–S trending valley formed by the long-term sinistral strike-slip activity of the Palu-Koro fault, and there are active faults developed in both the eastern and western margins of the basin. Palu-Koro is the main plate boundary structure that accommodates the relative motion between the Makassar block to the west and the North Sula block to the east (Walpersdorf *et al.* 1998). The strike-slip fault connects to the Minahassa subduction zone to the North, and to the Matano strike-slip fault to the south (Fig. 1b). The sinistral strike-slip Palu-Koro fault divides Sulawesi Island into two parts, and GPS data shows that the slip rate is 35 ± 8 mm a^{-1} (Bellier *et al.* 2001) and the locking depth is $\sim$12 km (Socquet *et al.* 2006; Walpersdorf *et al.* 1998; Stevens *et al.* 1999). Historic earthquake studies show that in the past 100 yr, there have been about 12 earthquakes of magnitude 6.5 or more occurring in Sulawesi Island (Vigny *et al.* 2002). The largest one out of these 12 earthquakes was the 1996 Tomini M_w 7.9 earthquake (Gomez *et al.*

© The Author(s) 2020. Published by Oxford University Press on behalf of The Royal Astronomical Society.

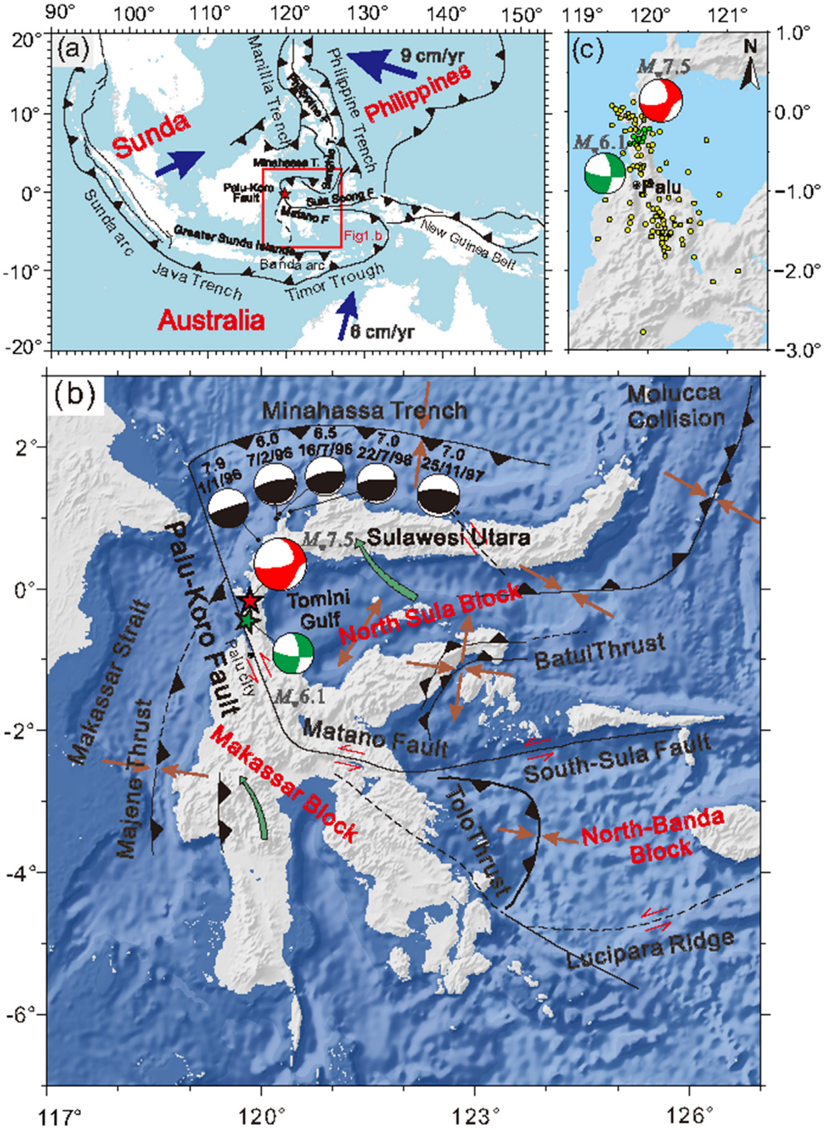

Figure 1. Tectonic setting. (a) Main plates and structures around Sulawesi Island (modified from Socquet *et al.* 2006). Straight and dark blue arrows show the magnitude and direction of the Australian and Philippine plates' velocities relative to Sundaland. (b) Regional plate tectonic map for the Sulawesi region of Indonesia (modified from Bellier *et al.* 2006). Black lines are the plate boundary faults. Triangles designate subduction zones. Brown arrows show relative plate motion across these faults. Curved and green arrows depict the rotation of the Sula block towards the Minahassa trench, and the associated counter rotation of the South Sulawesi block relative to Sundaland. The red and green five-pointed stars denote the epicentre locations of the main shock and the largest foreshock. The red and green beach-balls are the focal mechanism solutions of the mains hock and foreshock, respectively. The black beach-balls depict only earthquakes of magnitude larger than 6 between 1 January 1991 and 1 June 2000 occurred on Minahassa trench. Focal mechanisms are from GCMT catalogue. (c) Foreshocks and aftershocks with magnitude above 4 within 24 hr before and after the earthquake (data from USGS catalogue). The green dots indicate foreshocks and the yellow dots indicate aftershocks.

2000) with an epicentre of ∼120 km north of the earthquake studied in this paper, and it occurred in the Minahassa Trench subduction zone and was a thrust-type rupture event (Fig. 1b). The high slip rate and shallow locking of the Palu-Koro fault make the area have high risk of strong earthquake (Walpersdorf *et al.* 1998).

The source rupture process of large earthquakes can show the whole rupture duration, rupture scale and total energy released, as well as the spatial distribution of slip on the rupture surface and the kinematic process of seismic moment with time (Kikuchi & Kanamori 1991). Thus, we can calculate the changes in deformation and static Coulomb stress change in the surface and at a certain underground depth according to the slip distribution model of the seismic fault, and then evaluate the damage degree of surface buildings caused by the earthquake and the influences of the earthquake on the active faults in and around potential focal areas (King *et al.* 1994; Stein 1999; Parsons *et al.* 2008). For marine earthquakes, thrust faults or normal faults are one of the main causes of tsunamis (Kanamori 1972). The deformation of seabed can be calculated based on the slip distribution model of seismic faults, and then tsunami simulation can be carried out to realize tsunami warning (Titov *et al.* 2005; Kanamori & Rivera 2008). The Palu earthquake represents one of the first instances in which both the shallow and deeper slip can be very well resolved for a mature continental plate-boundary strike-slip fault (Socquet *et al.* 2019). The evidences from both seismology and geodesy suggest that the Palu earthquake is a supershear rupture event (Bao *et al.* 2019; Fang *et al.* 2019; Li *et al.* 2019; Socquet *et al.* 2019). The supershear earthquake will result in more strong shaking at large distance to the fault plane rather than intensive near-fault field ground motion, which is attributable to the generation of *S*-wave Mach front, which can persist farther distance and the seismic energy transmitted further with large amplitudes, which will definitely exacerbate the hazard (Dunham 2005; Bao *et al.* 2019; Fang *et al.* 2019). The M_w 7.5 earthquake in Palu, Indonesia, provides a good opportunity for us to study supershear rupture, Palu-Koro fault tectonic activity, regional seismic risk and even the causes of tsunami.

The back-projection (BP) method is simple and quick, and it can be used to study the relative magnitudes of focal rupture velocity and energy and the spatiotemporal distribution thereof (Ishii *et al.* 2005; Ishii 2011). The resolution of BP is determined by the aperture and density of stations within seismic arrays, as well as the slowness properties of the seismic phases utilized. Combining arrays or phases can significantly improve resolution (Kiser & Ishii 2017). After the Palu earthquake in Indonesia, Bao *et al.* (2019) studied the source rupture process of this earthquake using the BP method with the far-field body waves obtained by the Australian seismic network. Their result reveals that the 2018 M_w 7.5 Palu earthquake was supershear rupture event from early on, with an average rupture speed of 4.1 km s^{-1}. Abundant observation data is an important guarantee to obtain the details of source rupture (Kiser & Ishii 2017). The data provided by Australian seismic network is limited, and the application of combined seismograph networks in the study with the BP method provides an useful way to enrich the data.

The BP method cannot determine the real energy magnitude and rupture slip distribution (Kiser & Ishii 2017). The finite fault inversion method (FFM) came into being earlier than the BP method. This method can determine the spatiotemporal distribution of focal rupture slip, and it has been quite mature and widely used (Kikuchi & Kanamori 1991). Socquet *et al.* (2019) and Song *et al.* (2019) obtained the coseismic deformation caused by the earthquake through calculation with the InSAR data, and inverted the static coseismic rupture slip distribution of the earthquake, but study on the kinematic rupture process of the earthquake needs to be deepened. According to the statistics by USGS, there were 12 foreshocks with magnitude 4 or more before the Palu earthquake. The largest foreshock (M_w 6.1) occurred ∼3 hr before the main shock, and is located at ∼20 km south of the main shock, with source type being the same as that of the main shock (Fig. 1c). The maximum aftershock moment magnitude is 5.8. The Palu earthquake not only triggered a tsunami, but also caused soil liquefaction in the Palu basin (Socquet *et al.* 2019). Influenced by the foreshocks and aftershocks, as well as the tsunamis and soil liquefaction, the surface deformation calculated from the data of synthetic aperture radar (SAR) and optical images is not entirely caused by the main shock, and the error is difficult to eliminate. In addition, partial rupture of the Palu earthquake occurred in the bay, so it is difficult to obtain the seabed deformation caused by this segment of rupture by means of observation of synthetic aperture radar (SAR) and optical images. Furthermore, the kinematic source rupture process cannot be obtained from the static near-field deformation data. The high frequency seismic wave data recorded by the Incorporated Research Institutions for Seismology (IRIS, http://ds.iris.edu/ds/nodes/dmc/data/) provides reliable data support for the study on the focal rupture process of this earthquake. The USGS corrected the focal location and origin time of this earthquake on 1 December 2018 by moving the epicentre ∼8 km southwards (Fig. 2a), increasing the focal depth from 10 to 20 km, and delaying the origin time by ∼1.8 s. BP method requires little a prior information to be applied, which facilitates the study of complex rupture properties including segmentation, multiple-fault triggering and frequency dependence (Ishii *et al.* 2004; Kiser & Ishii 2017). However, the accuracy of the focal location, origin time and rupture velocity, which are used as the prior information for obtaining the source rupture process, is crucial for the results of finite fault inversion (Olson & Apsel 1982; Zhang 2008).

Therefore, this paper took the corrected focal location and origin time as prior information. First, the far-field body wave data with high signal-to-noise ratio from the combined seismograph networks was collected, and then the velocity and spatiotemporal distribution of rupture were researched using the BP method. Secondly, the source rupture process of the earthquake was studied using the FFM, with the rupture velocity obtained by the BP method as known condition, and the far-field body wave collected from the IRIS as constraints. Finally, the results obtained with these two methods were compared and analysed comprehensively, giving a complete and reliable spatiotemporal evolution process of focal rupture of the Palu earthquake.

2 METHOD AND RESULTS

2.1 Back-projection method

BP method is a type of array processing that images the source of seismic waves coherently recorded at stations throughout the seismic network (Kiser & Ishii, 2017). The method is characterized by stable results, high positioning accuracy and fast calculation speed, etc., and it can be used to quickly estimate such kinematic parameters as rupture zone, rupture duration, and rupture velocity (Wang & Mori 2011; Kiser & Ishii 2017). Another advantage of the method is that it can be used to process data at almost all frequencies, even data at high frequency more than 1.0 Hz (Koper *et al.* 2011, 2012; Kiser & Ishii 2017). High-frequency seismic signals, such as rapid changes in rupture acceleration and slip amplitude, have important guiding significance in the study on structure and seismic dynamics in seismic engineering (Campillo *et al.* 1989). However, the BP method cannot be used for effective quantitative calculation for the Green's function which affects the regional distribution of seismic wave energy (Ishii *et al.* 2005), so that the estimation of the actual slip distribution or seismic moment density distribution cannot be obtained using this method.

The BP method is a signal delay superposition method, and its core idea is to discretize the energy released by an earthquake into many subevents (Ishii *et al.* 2005; Kiser & Ishii 2017). The focal area is gridded, each grid node is regarded as a possible rupture event, and the theoretical traveltime of *P* wave from a grid node to each station in the network is calculated. The seismic wave from each station is translated to the time of the grid node according to the theoretical traveltime difference and the obtained seismic waves are superimposed. The superimposed waveform is intercepted by a time window and a slip time step, and then the energies radiated at different time points at the grid node are obtained by accumulating the waveforms in the time window. The grid node with the largest energy at a time point is the rupture front at this time point. Eq. (1) gives the superposition method for calculating the energy radiated

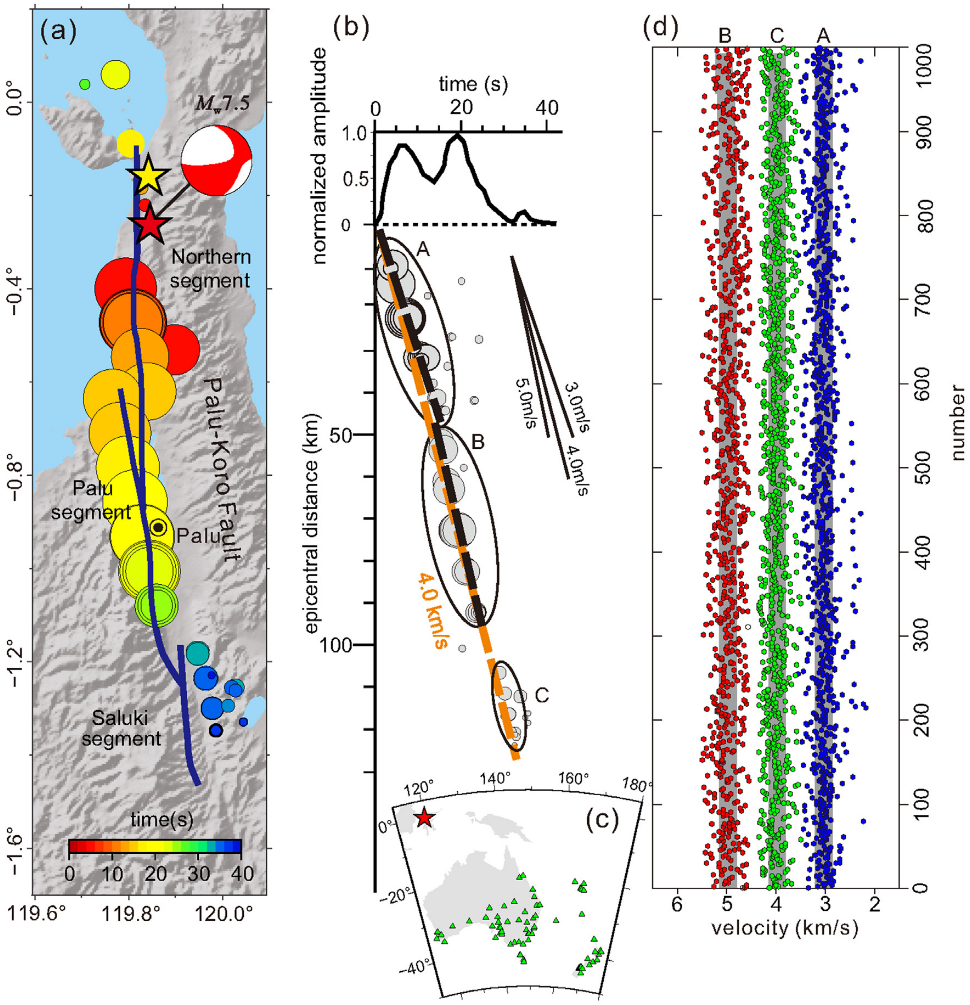

Figure 2. Source rupture process of Palu earthquake. (a) Spatial distribution of energy released by the Palu earthquake. The gray circles denote the energy released by the earthquake; the yellow five-pointed star is the epicentre location determined by USGS before correction, and the red five-pointed star is the epicentre location after correction; (b) Focal rupture process obtained using the back-projection method. The black curve is the source time function obtained using the back-projection method; (c) Distribution of stations in the combined network. The red five-pointed star is the epicentre location; the green triangles represent the station locations; (d) Rupture velocity distribution diagram obtained from 1000 random tests using the back-projection method with 40 stations selected from 84 ones. The blue dots are the rupture velocity values in segment A (average ~3.05 km s^{-1}), the red dots are the rupture velocity values in segment B (average ~4.98 km s^{-1}), and the green dots are the rupture velocity values in segment C (average ~4.03 km s^{-1}).

in each subevent—the *N*th root superposition method.

$$\begin{cases} \acute{S}_i(t) = \dfrac{1}{M} \sum_j^M w_j \left| u_j \left(t + t_{ij}^P + \Delta t\right)\right|^{1/n} \dfrac{u_j}{|u_j|} \\ S_i(t) = \left|\acute{S}_i(t)\right|^n \dfrac{\acute{S}_i(t)}{\left|\acute{S}_i(t)\right|}, \end{cases} \tag{1}$$

where u_j is the vertical waveform record at the jth station, t_{ij}^P is the theoretical traveltime of direct P wave from the jth station to the ith grid node, Δt is the time correction for the jth station relative to the reference station, of which the purpose is to remove the influence of medium inhomogeneity on the theoretical arrival time, w_j is the weight for the jth station, and M is the total number of stations involved in the calculation. When $n = 1$, eq. (1) is linear superposition. Linear superposition cannot improve signal-to-noise ratio, while high-order root superposition can weaken the spikes or glitches in a waveform, to better enhance the signal energy and suppress the noise interference (Ishii *et al.* 2005). Fourth-order root superposition algorithm, namely $n = 4$, is usually used.

In this paper, when the focal area was gridded, the epicentre was set to 119.846°E and 0.256°E, the fault strike was 348°, the focal depth was 20 km and 33 and 21 grid nodes were set at intervals of 10 km along the strike direction and dip direction, respectively. The higher the frequency of P wave, the higher the spatial resolution of the rupture front in the rupture process of earthquake, but the higher the frequency of seismic signal, the lower the similarity between the homologous signals at different stations, so the optimal frequency range 0.2−1.0 Hz was selected with various factors being comprehensively taken into account. In this frequency range, the horizontal resolution and waveform continuity achieved the best balance for obtaining optimal focal images. Bao *et al.* (2019) believed through comparative analysis that the Australian seismic network was more suitable for studying the source parameters of the Palu earthquake with the back-projection method. To obtain more abundant observation data, 84 stations with azimuth angle and epicentre distance falling in the ranges of 115−190° and 30−65°, respectively were selected to form a combined network, covering the Australian seismic network. The seismic waves within the epicentre distance range mainly propagated in the lower mantle with relatively homogeneous medium, effectively weakening the influence of the inhomogeneity of materials in the crust, upper mantle and core–mantle boundary. To eliminate the influence of different types of instruments in different networks, the instrument response was deducted from the original observation data. The minimum traveltime difference between PP and P seismic phases is 71 s. Since the PP phase might interfere with the focal rupture imaging and the signal-to-noise ratio of vertical component P wave was higher than in the horizontal component, the 1-D velocity model IASP91 was used to calculate the theoretical arrival time of direct P wave, and a total of 80 s of vertical component waveform data was intercepted, including 10 s before and 70 s after the arrival time of direct P wave used as the reference time. Owing to the inhomogeneity of the earth medium, there was a deviation between the actual arrival time of direct P wave and the theoretical arrival time The correlation test was conducted for a total of 15 s of waveform, including 5 s before and 10 s after the arrival time of direct P wave, with the correlation coefficient agreed as 0.65, and the arrival time of direct P wave was corrected using the cross-correlation technique. After the stations with poor signal-to-noise ratio for vertical component waveform and those with poor correlation were removed, there were 71 stations finally left for vertical component waveform (Fig. 2c).

Our result (Fig. 2) shows that the rupture of 2018 M_w 7.5 Palu earthquake mainly propagated southwards, resulting in a rupture length of ~150 km (0.2°S–1.4°S) on the south side of epicentre. The rupture also occurred on the north side (0.1°N–0.2°S), indicating that the earthquake is not a simple unilateral rupture event. The whole rupture process performed in two main stages: (1) bilateral rupture stage and (2) unilateral rupture stage. Coseismic deformation map derived from InSAR data (Fang *et al.* 2019; Socquet *et al.* 2019; Song *et al.* 2019; Ulrich *et al.* 2019) and early aftershocks recorded by USGS (Fig. 1c) clearly indicate a long rupture extension of the Palu earthquake (over 150 km), which agrees with our result. The non-linear spatial distribution of energy suggests that the seismogenic fault is composed of multiple segments, coinciding with the result of Ulrich *et al.* (2019). There are at least three visible slip patches on the fault plane. The rupture lasted for about 40 s. There are three rupture peak zones near 7th s, 19th s and 35th s, and they correspond to three energy concentration zones, respectively, which are located within 0–50 km, 50–100 km and 105–125 km on the south side of the epicentre, respectively (referred to as segment A, segment B and segment C for short). The rupture velocity along strike is ~3.0 km s^{-1} in segment A, ~5.0 km s^{-1} in segment B and ~4.0 km s^{-1} in segment C. The average rupture velocity in the whole rupture process is about 4.0 km s^{-1}, which is consistent with results of Bao *et al.* (2019) and Fang *et al.* (2019). To verify the reliability of the above calculation results, the source rupture process of the Palu earthquake was recalculated using the BP method, with 40 stations randomly selected from 84 ones. Statistical experimental study shows that the calculation result in this paper is robust (Fig. 2d).

2.2 Finite fault inversion method

The finite fault inversion method has a long history. The inversion of source rupture process mainly depends on seismic waves. With the rapid development of space geodetic technology, especially the high frequency GNSS technology, geodetic data has been widely used in study on focal rupture process (Atzori *et al.* 2009; Wang *et al.* 2011; Crowell *et al.* 2012). The finite fault inversion method can be used to obtain detailed spatiotemporal distribution of focal rupture (Xu *et al.* 2009; Song *et al.* 2019), and it makes up for the defect of the back-projection method. The theoretical Green's function from the source to each station was calculated by assuming an initial source model and believing that the region where the ray paths pass through from the source to the stations has a known velocity structure (Olson & Apsel 1982). If we want to obtain the time process of source rupture, we often need to assume the initial rupture point and rupture velocity, and constrain the shape of source–time function of each subevent (Olson & Apsel 1982). As shown in eq. (2), the simulation values are fitted with the observation values, and the optimal approximation values of source parameters are obtained by reducing the residual errors res between the theoretical values and the actual observation values through constant correction of the coefficient matrix m of the source model in an iterative manner.

$$\begin{cases} u_n\ (t) = \sum_i^K \sum_J^M \left[m_{ij}^1 \cdot g_{nj}^1\left(\vec{x}_j, t\right) + m_{ij}^2 \cdot g_{nj}^2\left(\vec{x}_j, t\right)\right] * s_{ij}\,(t) \\ \quad ||\omega\,(G \cdot m - obs)\,||^2 + \beta^2 ||L \cdot m||^2 = res, \end{cases} \tag{2}$$

where $u_n(t)$ is the displacement response at the station $\vec{x}_j$; M is the total number of subfaults; K is the number of time windows corresponding to each subfault; m_{ij} is the slip corresponding to the ith time window of the jth subfault, 1 denotes the component along the strike-slip direction and 2 denotes the component along the dip-slip direction; $g_{nj}(\vec{x}_j, t)$ is the displacement response of the unit slip of the jth subfault at the station $\vec{x}_j$, 1 denotes along the strike-slip direction and 2 denotes along the dip-slip direction, so the total number of unknown variables is $2 \cdot M \cdot K$; $s_{ij}\,(t) = \frac{1-\cos(2\pi t/d)}{d}$ represents the shape of a time window, and d is the width of the time window; obs denotes an observation value; $G \cdot m = u$ denotes a simulation value, and $G = g * s$; m is the slip to be calculated; and ω is the weight of an observation value, and $\omega = 1$ for a single type of data. Earthquake rupture is typically continuous, and its smoothness can be described with Laplace second-order difference operator L and smoothing factor β.

According to the GCMT measurements, the strike, dip angle and slip angle of seismogenic fault of the Palu earthquake occurring in Indonesia in September 2018 are 348°, 57° and –15°, respectively. We assumed a single fault plane, whose geometry has been chosen based on the focal mechanism solution determined by GCMT. We extended the size of fault plane to be 240 km × 28 km and discretized it into 60 subfaults in the strike direction and 7 subfaults in the dip direction, with each subfault path size of 4 km × 4 km (Fig. 3a). The initial rupture point (119.846°E, 0.256°S, 20.0 km) is located at (0, 0), which is the latest focal location after correction. According to the results obtained by the BP method, the rupture velocity along the strike of the fault was set to 3.0 km s^{-1} in the first 50 km, then continues to propagate at a speed of 5.0 km s^{-1} for 50 km, and finally the rupture velocity changes to 4.0 km s^{-1}. We used Global Seismographic Network (GSN, https://www.iris.edu/hq/programs/gsn/) broad-band waveforms downloaded from the NEIC waveform server. We analysed 32 teleseismic broadband P waveforms selected based on data quality and azimuthal distribution (Fig. 3c). Waveforms are first converted to displacement by removing the instrument response and are then used to constrain the slip history using a finite fault inverse algorithm. The origin time was the latest result after correction by the USGS, and a total of 60 s of waveform data was intercepted, including 5 s before and 55 s after the arrival time of direct P wave used as the reference time. The waveform was processed first to

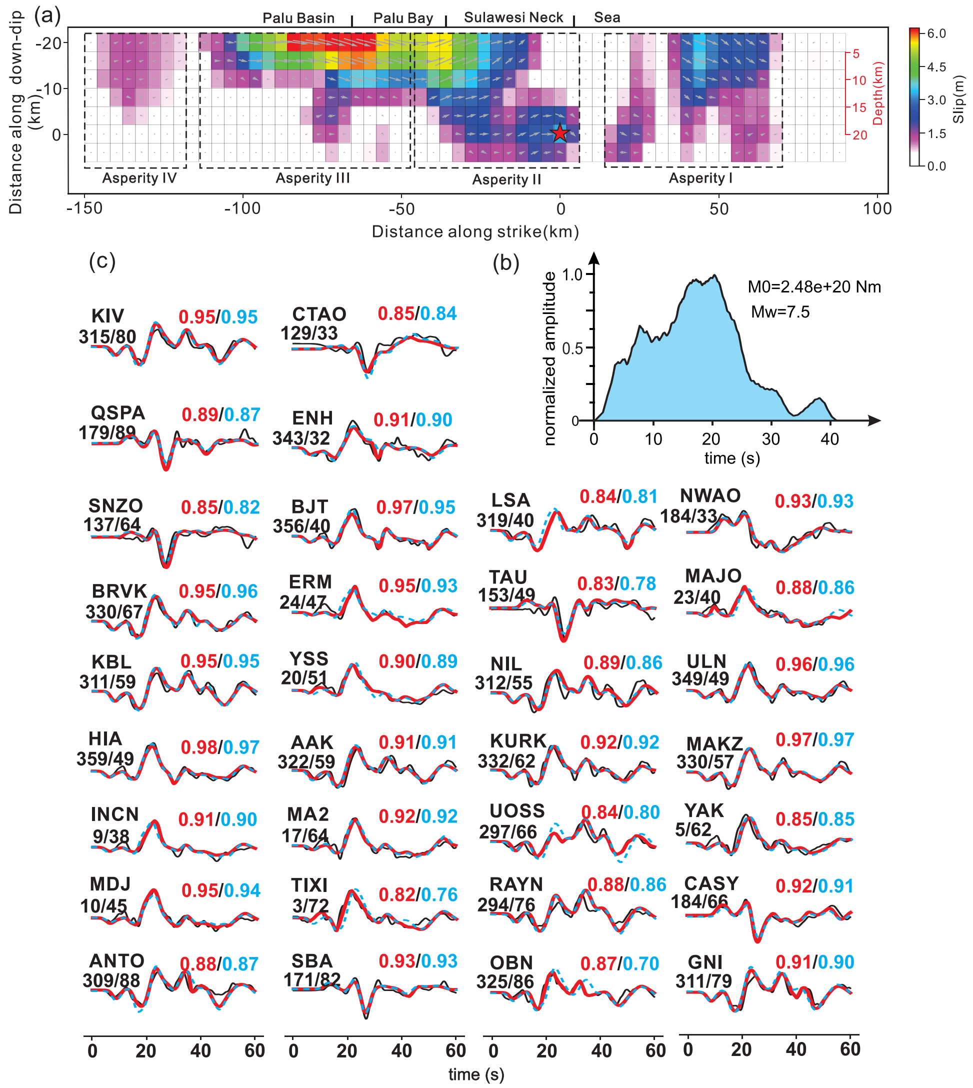

Figure 3. Coseismic rupture model of Palu earthquake. (a) Evolution process of the rupture and slip distribution of the Palu earthquake with time. The red five-pointed star is the initial rupture point, that is, the focal location. (b) Source time function. (c) Observed and simulated waveforms. The black curves represent the observation values. The blue dotted line is the simulated value at a uniform rupture velocity (4.0 km s^{-1}). The red solid line is the simulated value at non-uniform rupture speed. The station name, epicentre distance and azimuth angle are shown on the left-hand side. The correlation coefficients are shown on the right-hand side.

remove instrument response, and the signal in the frequency range of 0.01 − 1.0 Hz was extracted threw bandpass filtering.

To examine the fault rupture model, a non-negative least-squares (NNLS) method was used to inverted the far-field wave data for the rupture process on the fault plane, which minimize the *res* misfit between the data and the model (eq. 2). Trying to explain the misfit and check the non-uniformity of the rupture velocity, we re-inverted the source rupture process with a uniform rupture velocity of 4.0 km s^{-1}. The inversion result shows that the model can better fit the data when non-uniform rupture speed was used (Fig. 3c). In consistent with the focal mechanism solutions, the slip distribution on the fault plane presents four predominant slip patches, where the motion is dominated by strike-slip with normal-slip components as well (Fig. 3a). Significant normal-slip components are observed in asperity I and III. However, obvious thrust slip occurred at asperity II and IV, which is consistent with the result given by USGS. Fang *et al.* (2019) held that the thrust slip observed at asperity II connects to the North Sulawesi trench where subduction occurs and the thrust-slip in asperity IV is likely due to the geometric complexity of the fault bends where the rupture terminated (Fig. 1b). The rupture lasted for nearly 42 s, releasing a total seismic moment of 2.48 × 10^{20} Nm (M_w 7.5), most of which was released within the first 32 s (Fig. 3b). The spatial-temporal slip evolution (Fig. 4) demonstrates that the rupture propagated bilaterally towards the north and south during the first 24 s, and then to the south, resulting in four visible asperities as illustrated in the total slip distribution (Fig. 3), which corresponds to four lobes of deformation in the coseismic interferogram (Socquet *et al.* 2019). A maximum slip of ∼6.24 m was resolved on a shallow part of the crust near ∼60 km away from epicentre. The northern segment (asperity I and II) slipped at a greater depth down to 20 km, which agrees with the model of Socquet *et al.* (2019).

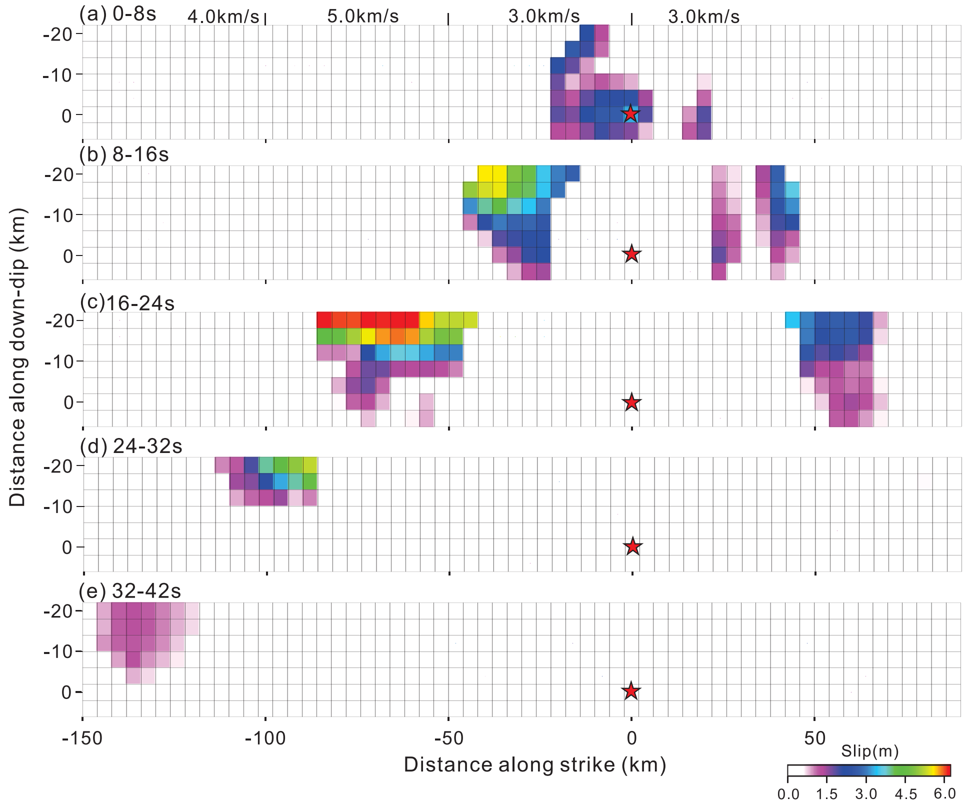

Figure 4. Snapshots of the rupture propagation. The red star represents the epicentre.

3 DISCUSSION

3.1 Supershear occurred in Palu bay and Palu basin

Our rupture process model reveals that the 2018 M_w 7.5 Palu earthquake is a supershear event. The local shear wave velocity ranges from 3.4 to 3.8 km s^{-1} between the depths of 3–20 km according to CRUST 1.0 model (Bao *et al.* 2019; Li *et al.* 2019). The rupture velocity is ~3.0 km s^{-1} in the first 50 km, ~5.0 km s^{-1} in the range of 50–100 km and 4.0 km s^{-1} for the last 20 km, indicating that the supershear occurred in south of Palu coastline (Fig. 2a). The statistical analysis proves that the rupture velocity determined by BP method is by no means accidental. The supershear feature has been validated by seismologic evidence of far-field Rayleigh Mach waves (Bao *et al.* 2019). Fang *et al.* (2019) further revealed the supershear rupture by a joint inversion of seismic and geodetic data. Ulrich *et al.* (2019) revealed the supershear rupture by a joint analysis of seismic, geodetic and tsunami records. Socquet *et al.* (2019) speculated through analysis of coseismic displacement that the supershear occurred in south of Palu coastline (that is, south of 0.9°S). Our preferred rupture model provides seismological evidence for the speculation. Our result determined by BP method suggests an average speed of ~4.0 km s^{-1} during the whole rupture process, which agrees with Bao *et al.* (2019), Fang *et al.* (2019) and Li *et al.* (2019), but smaller than the result of Ulrich *et al.* (2019) which demonstrated an average speed of 5.0 km s^{-1}. The findings of Bao *et al.* (2019) and Li *et al.* (2019) indicate that the rupture dose not extent toward the north side of the epicentre, coinciding with the modelling result of Ulrich *et al.* (2019). However, the geodetic data shows that the earthquake results in obvious displacement in this region (Fang *et al.* 2019; Socquet *et al.* 2019; Song *et al.* 2019). The rupture velocity of Li *et al.* (2019), based on the Hi-net array, is less satisfying due to the unfavorable interference between *P* phase an pP phase (Bao *et al.* 2019). Both Fang *et al.* (2019) and Bao *et al.* (2019) indicate that the Palu earthquake is an early and persistent supershear with the rupture speed of ~4.1 km s^{-1}. The coseismic slip model of Fang *et al.* (2019) does not fit the observation well, especially the broad-band regional seismograms. Only Australian seismic network is selected by Bao *et al.* (2019) to research the rupture process of the Palu earthquake. The New Zealand array, in the southeast of Australian seismic network, gives result that is overall consistent with that of the Australian seismic network array (Bao *et al.* 2019). Abundant observation data with good azimuth coverage is an important guarantee to obtain the details of source rupture (Kiser & Ishii, 2017). The application of combined seismograph networks in our study with the BP method is more reasonable. Reliability of the rupture speed can be reflected, to some extent, by fitness between observed waveforms and synthetic waveforms. Therefore, we calculated synthetic waveforms for 32 stations based on the spatio-temporal rupture model constrained by different rupture velocity. As shown in Fig. 3(c), the rupture model with non-uniform rupture velocity constraint better fits the observation data.

Bouchon *et al.* (2010) indicated that supershear rupture earthquakes are usually associated with faults that show simple geometry with small or even an absence of segmentation features. The surface traces of these faults are typically linear, continuous and narrow, as evidenced by the optical satellite images, suggesting that stress-strength of the fault plane is mechanically homogeneous (Fang *et al.* 2019). South of the Palu coastline (0.9°S), the north–south displacement (Bao *et al.* 2019; Socquet *et al.* 2019) shows a very sharp contrast between two side of the Palu fault, which suggests that the rupture occurs in a linear, narrow and smooth segment. North of Palu city, the rupture disappears offshore within the Palu bay, and reappears 21 km further north within the Sulawesi neck, where a much smoother displacement gradient can be followed northwards for 60 km (Socquet *et al.* 2019). It implies that a buried slip probably occurs on the segment, which is confirmed by our coseismic rupture model (Fig. 2a). However, the supershear slip of earthquakes, for example 1999 Izmit earthquake, 2001 Kunlun earthquake, 2002 Denali earthquake, 2010 Yushu earthquake, etc., occurred on the shallow part of strike-slip faults, which indicates that the supershear rupture occurred in the south of Palu coastline and Palu bay, not the Sulawesi neck (Fig. 2), is reasonable.

3.2 Slip distribution and rupture characteristics

As two main methods to study the source rupture process, the BP method and the FFM are independent yet verifiable and complementary. Both of them find that the rupture lasts about 40 s. The total seismic moment released is $\sim 2.48 \times 10^{20}$ Nm. Based on our model, we find that the rupture is mainly concentrated on the south side of the epicentre and also existed on the north side (Fang *et al.* 2019), which suggests that the 2018 M_w 7.5 Palu earthquake is not a simple unilateral rupture event, and the rupture mainly included two main stages.

Our rupture model shows that the Palu earthquake is a supershear event dominated by left-lateral strike-slip with both normal and thrust components as well, which agrees with the results of USGS, Socquet *et al.* (2019) and Fang *et al.* (2019). Four obvious asperities (Fig. 2a) are ruptured during the whole slip history, which agree with the results of USGS and Fang *et al.* (2019), but are not revealed in the models of Song *et al.* (2019) and Ulrich *et al.* (2019). The slip model of Song *et al.* (2019) shows that a large asperity with predominant normal slip is found on the north segment of epicentre, which shows good agreement with our model. Song *et al.* (2019) hold that the off-shore (asperity I) normal faulting likely favors tsunami genesis. Based on our model, the maximum normal-slip reaches 2.02 m around the Palu bay, coinciding with the results of Ulrich *et al.* (2019) and Fang *et al.* (2019), which probably is also responsible for the tsunami (Fang *et al.* 2019). Thrust slip component in our model is found in Sulawesi Neck and north part of Palu bay (asperity II), where a restraining bend has been formed (Ulrich *et al.* 2019), which is consistent with Socquet *et al.* (2019). However, no thrust slip is found in the model of Song *et al.* (2019), which is probably due to the fact that near-fault InSAR data are cut off in their inversion (Fang *et al.* 2019). Thrust slip, occurred on the Saluki segment (asperity IV), is likely due to geometrical complexities of the Palu-Koro fault bends which extend southwards with the Matano fault (Fang *et al.* 2019). The model of Song *et al.* (2019) reveals that slip on main fault plane presents two predominant slip patches above 20 km, where the motion is dominated by strike-slip with a maximum slip of $\sim$7.7 m except a normal component on the segment south of the Palu city. The slip on the northern (asperity I and II) and southern (asperity III and IV) segment in our rupture model expresses difference behaviors. The southern fault segment experience most of the moment release between 0 and 15 km depth, while the northern segment tended to slip at greater depth (down to 20 km), which is consistent with Socquet *et al.* (2019) and Fang *et al.* (2019). After the 2018 M_w 7.5 earthquake, USGS first collected the GSN broad-band waveforms to resolve the rupture process of Palu earthquake. Then, InSAR data was involved in the analysis of coseismic deformation and research of slip model (Socquet *et al.* 2019; Song *et al.* 2019). Fang *et al.* (2019) combined InSAR data and broadband regional seismograms to study the source rupture process. The model of USGS shows that the slip is too discrete, and the maximum slip is not consistent with the coseismic displacement. The residual maps of Socquet *et al.* (2019) show a large misfit in the Balaesang Peninsula and some LOS deformation areas that are either overfitted or underfitted (Fang *et al.* 2019). Although the slip model of Fang *et al.* (2019) has improved the situation, the broadband regional seismograms fits poorly, which implies that the weight of seismic data in the inversion is low. We should acknowledge that our simplified fault geometry with uniform dip angle may have some limitations. More accurate geometric parameters with more abundant data sets such as static and high-rate GPS measurements, strong motion data, teleseismic waveforms, and tsunami records will be favorable to refine a more detailed slip model and rupture (Socquet *et al.* 2019). Our model could be considered as a first approximation of the 2018 Palu earthquake.

4 CONCLUSIONS

We researched the rupture process for the 2018 M_w 7.5 Palu earthquake by inverting the far-field body waves. Both the back-projection method and the finite fault inversion method jointly revealed the complexity of the rupture process of the earthquake. We found that this earthquake has two main rupture stages. In the first stage, the rupture propagated southwards and northwards simultaneously and was a bilateral rupture, and the rupture occurred in both deep and shallow parts of the fault. In the second stage, the rupture mainly propagated southwards and was a unilateral rupture, and the rupture was concentrated in the shallow part of the fault. Our rupture model shows that the Palu earthquake is a supershear event dominated by left-lateral strike-slip with both normal and thrust components as well. The total seismic moment $\sim 2.48 \times 10^{20}$ Nm was released within $\sim$42 s. A maximum slip of $\sim$6.24 m was resolved on a shallow part of the crust near $\sim$60 km away from epicentre. The rupture velocity was non-uniform and the supershear occurred in the Palu bay and Palu basin.

We obtained the rupture process and slip model for the 2018 Sulawesi earthquake by inverting the far-field body waves. Both the back-projection method and the finite fault inversion method jointly revealed the complexity of the rupture process of the M_w 7.5 Palu earthquake in Indonesia in 2018. We found that this earthquake has two rupture stages. In the first stage, the rupture propagated southwards and northwards simultaneously and was a bilateral rupture, and the rupture occurred in both deep and shallow parts of the fault. In the second stage, the rupture mainly propagated southwards and was a unilateral rupture, and the rupture was concentrated in the shallow part of the fault. The second stage of rupture showed remarkable supershear rupture characteristics. At first, the rupture propagated along the fault at a relatively slow velocity. When the rupture jumped to adjacent fault, its velocity increased suddenly and it turned into supershear rupture. These results show that the back-projection method and the finite fault inversion method can complement and verify each other in studying the kinematic details of focal rupture. Our study has important implications for understanding the deformation mechanism in NW Sulawesi.

ACKNOWLEDGEMENTS

This work was supported by the National Key Research and Development Program of China (Number 2018YFC1503605), and by the Scientific Research Fund of Institute of Seismology and Institute of Crustal Dynamics, China Earthquake Administration (Number IS201856289). Most of the figures were plotted using Generic Mapping Tools (GMT) open-source collection of computer software tools (Wessel et al., 2013). We acknowledge helpful comments and suggestions provided by the anonymous reviewer which improved the content of this paper.

REFERENCES

Atzori, S. *et al.* 2009. Finite fault inversion of DInSAR coseismic displacement of the 2009 L'Aquila earthquake (central Italy), *Geophys. Res. Lett.,* **36,** L15305, doi: 10.1029/2009GL039293.

Bao, H., Ampuero, J.P., Meng, L., Fielding, E.J., Liang, C., Milliner, C.W., Feng, T. & Huang, H., 2019. Early and persistent supershear rupture of the 2018 magnitude 7.5 Palu earthquake, *Nat. Geosci.,* **12,** 200–205, doi: 10.1038/s41561-018-0297-z.

Bellier, O. *et al.* 2006. Fission track and fault kinematics analyses for new insight into the Late Cenozoic tectonic regime changes in West-Central Sulawesi (Indonesia), *Tectonophysics,* **413,** 201–220, doi: 10.1016/j.tecto.2005.10.036.

Bellier, O., Sébrier, M., Beaudouin, T., Villeneuve, M., Braucher, R., Bourlès, D. L., Siame, L. L., Putranto, E. & Pratomo, I. 2001. High slip rate for a low seismicity along the Palu-Koro active fault in central Sulawesi (Indonesia), *Terra Nova,* **13,** 463–470, doi: 10.1046/j.1365-3121.2001.00382.x.

Bouchon, M. *et al.* 2010. Faulting characteristics of supershear earthquakes, *Tectonophysics,* **493,** 244–253, doi: 10.1016/j.tecto.2010.06.011.

Campillo, M., Gariel, J.C., Aki, K. & Sanchez-Sesma, F.J., 1989. Destructive strong ground motion in Mexico City: source, path, and site effects during great 1985 Michoacán earthquake, *Bull. seism. Soc. Am.,* **79,** 1718–1735.

Crowell, B.W., Bock, Y. & Melgar, D., 2012. Real-time inversion of GPS data for finite fault modeling and rapid hazard assessment, *Geophys. Res. Lett.,* **39,** doi: 10.1029/2012GL051318.

Dunham, E.M., 2005, The dynamics and near-source ground motion of supershear earthquakes, *PhD thesis*, University of California, Santa Barbara.

Fang, J., Xu, C.J., Wen, Y.M., Wang, S., Xu, G.Y., Zhao, Y.W. & Yi, L., 2019. The 2018 Mw 7.5 Palu earthquake: a supershear rupture event constrained by InSAR and Broadband regional seismograms, *Remote Sens.,* **11,** 1330, doi: 10.3390/rs11111330.

Gómez-González, J.M., Madariaga, R., Walpersdorf, A. & Chalard, E., 2000. The 1996 earthquakes in Sulawesi, Indonesia, *Bull. seism. Soc. Am.,* **90,** 739–751, .

Ishii, M., 2011. High-frequency rupture properties of the Mw 9.0 off the Pacific coast of Tohoku Earthquake, *Earth Planet Space,* **63,** doi: 10.5047/eps.2011.07.009.

Ishii, M., Shearer, P.M., Houston, H. & Vidale, J.E. 2005. Extent, duration and speed of the 2004 Sumatra–Andaman earthquake imaged by the Hi-Net array, *Nature* **435,** 933–936, doi: 10.1038/nature03675.

Kanamori, H., 1972. Mechanism of tsunami earthquakes, *Phys. Earth planet. Inter.,* **6,** 346–359.

Kanamori, H. & Rivera, L., 2008. Source inversion of Wphase: speeding up seismic tsunami warning, *Geophys. J. Int.,* **175,** 222–238, doi: 10.1111/j.1365-246X.2008.03887.x.

Kikuchi, M. & Kanamori, H., 1991. Inversion of complex body waves-III, *Bull. seism. Soc. Am.,* **81,** 2335–2350.

King, G.C., Stein, R.S. & Lin, J., 1994. Static stress changes and the triggering of earthquakes, *Bull. seism. Soc. Am.,* **84,** 935–953.

Kiser, E. & Ishii, M., 2017. Back-projection imaging of earthquakes, *Annu. Rev. Earth planet. Sci.,* **45,** 271–299, doi: 10.1146/annurev-earth-063016-015801.

Koper, K.D., Hutko, A.R., Lay, T., Ammon, C.J. & Kanamori, H., 2011. Frequency-dependent rupture process of the 2011 Mw 9.0 Tohoku Earthquake: comparison of short-period P wave backprojection images and broadband seismic rupture models, *Earth Planet. Space,* **63,** 599–602, doi:10.5047/eps.2011.05.026.

Koper, K.D., Hutko, A.R., Lay, T. & Sufri, O., 2012. Imaging short-period seismic radiation from the 27 February 2010 Chile (Mw 8.8) earthquake by back-projection of P, PP, and PKIKP waves, *J. geophys. Res.,* **117,** B02308, doi:10.1029/2011JB008576.

Li, Q., Tan, K., Zhao, B., Lu, X.F., Zhang, C.H. & Wang, D.Z., 2019. The 2018 Mw 7.5 Palu, Indonesia earthquake: a supershear rupturing event, *Chinese J. Geophys.* (in Chinese), **62,** 3017–3023, doi: 10.6038/cjg2019M0616.

Mai, P.M., , 2019. Superhear tsunami disaster, *Nat. Geosci.,* **12,** 150–151, doi:10.1038/s41561-019-0308-8.

Olson, A.H. & Apsel, R.J., 1982. Finite faults and inverse theory with applications to the 1979 Imperial Valley earthquake, *Bull. seism. Soc. Am.,* **72,** 1969–2001.

Parsons, T., Ji, C. & Kirby, E., 2008. Stress changes from the 2008 Wenchuan earthquake and increased hazard in the Sichuan basin, *Nature,* **454,** 509–510, doi: 10.1038/nature07177.

Prasetya, G.S., De Lange, W.P. & Healy, T.R., 2001. The Makassar strait tsunamigenic region, Indonesia, *Nat. Hazards,* **24,** 295–307, doi: 10.1023/A:1012297413280.

Puntodewo, S.S.O. *et al.* 1994. GPS measurements of crustal deformation within the Pacific-Australia plate boundary zone in Irian Jaya, Indonesia, *Tectonophysics,* **237,** 141–153, doi: 10.1016/0040-1951(94)90251-8.

Rangin, C., Le Pichon, X., Mazzotti, S., Pubellier, M., Chamot-Rooke, N., Aurelio, M., Walpersdorf, A. & Quebral, R., 1999. Plate convergence measured by GPS across the Sundaland/Philippine Sea plate deformed boundary: the Philippines and eastern Indonesia, *Geophys. J. Int.,* **139,** 296–316, doi: 10.1046/j.1365-246x.1999.00969.x.

Socquet, A., Hollingsworth, J., Pathier, E. & Bouchon, M., 2019. Evidence of supershear during the 2018 magnitude 7.5 Palu earthquake from space geodesy, *Nat. Geosci.,* **12,** 192–199, doi: 10.1038/s41561-018-0296-0.

Socquet, A., Simons, W., Vigny, C., McCaffrey, R., Subarya, C., Sarsito, D., Ambrosius, B. & Spakman, W., 2006. Microblock rotations and fault coupling in SE Asia triple junction (Sulawesi, Indonesia) from GPS and earthquake slip vector data, *J. geophys. Res.,* **111,** doi: 10.1029/2005JB003963.

Song, X. G., Zhang, Y. F., Shan, X. J., Liu, Y. H, Gong, W. Y. & Qu, C. Y., 2019. Geodetic observations of the 2018 Mw 7.5 Sulawesi earthquake and its implications for the kinematics of the Palu fault, *Geophys. Res. Lett.,* **46,** 4212–4220, doi: 10.1029/2019GL082045.

Stein, R.S., 1999. The role of stress transfer in earthquake occurrence, *Nature,* **402,** 605–609, doi: 10.1038/45144.

Stevens, C., McCaffrey, R., Bock, Y., Genrich, J., Subarya, C., Puntodewo, S.S.O. & Vigny, C., 1999. Rapid rotations about a vertical axis in a collisional setting revealed by the Palu fault, Sulawesi, Indonesia, *Geophys. Res. Lett.,* **26,** 2677–2680, doi: 10.1029/1999GL008344.

Titov, V.V., Gonzalez, F.I., Bernard, E.N., Eble, M.C., Mofjeld, H.O., Newman, J.C. & Venturato, A.J., 2005. Real-time tsunami forecasting: challenges and solutions, *Nat. Hazards,* **35,** 35–41, doi: 10.1007/s11069-004-2403-3.

Ulrich, T. *et al.* 2019. Coupled, physics-based modeling reveals earthquake displacements are critical to the 2018 Palu, Sulawesi Tsunami, *Pure Appl. Geophys.,* **176,** 4069–4109, doi:10.1007/s00024-019-02290-5.

Vigny, C. *et al.* 2002. Migration of seismicity and earthquake interactions monitored by GPS in SE Asia triple junction: Sulawesi, Indonesia, *J. geophys. Res.,* **107,** ETG–7-1-ETG-7-11, doi: 10.1029/2001JB000377.

Walpersdorf, A., Vigny, C., Subarya, C. & Manurung, P., 1998. Monitoring of the Palu-Koro Fault (Sulawesi) by GPS, *Geophys. Res. Lett.,* **25,** 2313–2316, doi: 10.1029/98GL01799.

Wang, D. & Mori, J., 2011. Rupture process of the 2011 off the Pacific coast of Tohoku Earthquake (Mw 9.0) as imaged with back-projection of teleseismic P-waves, *Earth Planet. Space,* **63,** 603–607, doi: 10.5047/eps.2011.05.029.

Wang, Q. *et al.* 2011. Rupture of deep faults in the 2008 Wenchuan earthquake and uplift of the Longmen Shan, *Nat. Geosci.,* **4,** 634–640, doi: 10.1038/ngeo1210.

Watkinson, I.M. & Hall, R., 2016. Fault systems of the eastern Indonesian triple junction: evaluation of quaternary activity and implications for seismic hazards, *Geol. Soc., Lond., Spec. Publ.,* **441,** 71–120, doi: 10.1144/SP441.8.

Weseel, P., ,Smith, W. H. F. Scharroo, R., Luis, J. & Wobbe, F., 2013. Generic Mapping Tools: Improved Version Released *Eos, EOS Trans. AGU.,* **94,** 409–410, doi: 10.1002/2013EO450001.

Xu, X., Wen, X., Yu, G., Chen, G., Klinger, Y., Hubbard, J. & Shaw, J., 2009. Coseismic reverse-and oblique-slip surface faulting generated by the 2008 Mw 7.9 Wenchuan earthquake, China, *Geology,* **37,** 515–518, 10.1130/G25462A.1.

Zhang, Y., 2008, Study on the inversion methods of source rupture process, *PhD thesis* (in Chinese), Peking University.

Key words

Authors are requested to choose key words from the list below to describe their work. The key words will be printed underneath the summary and are useful for readers and researchers. Key words should be separated by a semi-colon and listed in the order that they appear in this list. An article should contain no more than six key words.

COMPOSITION and PHYSICAL PROPERTIES
Composition and structure of the continental crust
Composition and structure of the core
Composition and structure of the mantle
Composition and structure of the oceanic crust
Composition of the planets
Creep and deformation
Defects
Elasticity and anelasticity
Electrical properties
Equations of state
Fault zone rheology
Fracture and flow
Friction
High-pressure behaviour
Magnetic properties
Microstructure
Permeability and porosity
Phase transitions
Plasticity, diffusion, and creep

GENERAL SUBJECTS
Core
Gas and hydrate systems
Geomechanics
Geomorphology
Glaciology
Heat flow
Hydrogeophysics
Hydrology
Hydrothermal systems
Infrasound
Instrumental noise
Ionosphere/atmosphere interactions
Ionosphere/magnetosphere interactions
Mantle processes
Ocean drilling
Structure of the Earth
Thermochronology
Tsunamis
Ultra-high pressure metamorphism
Ultra-high temperature metamorphism

GEODESY and GRAVITY
Acoustic-gravity waves
Earth rotation variations
Geodetic instrumentation
Geopotential theory
Global change from geodesy
Gravity anomalies and Earth structure
Loading of the Earth
Lunar and planetary geodesy and gravity
Plate motions
Radar interferometry
Reference systems
Satellite geodesy
Satellite gravity
Sea level change
Seismic cycle
Space geodetic surveys
Tides and planetary waves
Time variable gravity
Transient deformation

GEOGRAPHIC LOCATION
Africa
Antarctica
Arctic region
Asia
Atlantic Ocean
Australia
Europe
Indian Ocean
Japan
New Zealand
North America
Pacific Ocean
South America

GEOMAGNETISM and ELECTROMAGNETISM
Archaeomagnetism
Biogenic magnetic minerals
Controlled source electromagnetics (CSEM)
Dynamo: theories and simulations
Electrical anisotropy
Electrical resistivity tomography (ERT)
Electromagnetic theory
Environmental magnetism
Geomagnetic excursions
Geomagnetic induction
Ground penetrating radar
Magnetic anomalies: modelling and interpretation
Magnetic fabrics and anisotropy
Magnetic field variations through time
Magnetic mineralogy and petrology
Magnetostratigraphy
Magnetotellurics
Marine electromagnetics
Marine magnetics and palaeomagnetics
Non-linear electromagnetics
Palaeointensity
Palaeomagnetic secular variation
Palaeomagnetism
Rapid time variations
Remagnetization
Reversals: process, time scale, magnetostratigraphy
Rock and mineral magnetism
Satellite magnetics

GEOPHYSICAL METHODS
Downhole methods
Fourier analysis
Fractals and multifractals
Image processing
Instability analysis
Interferometry
Inverse theory
Joint inversion
Neural networks, fuzzy logic
Non-linear differential equations
Numerical approximations and analysis
Numerical modelling
Numerical solutions
Persistence, memory, correlations, clustering
Probabilistic forecasting
Probability distributions
Self-organization
Spatial analysis
Statistical methods
Thermobarometry
Time-series analysis
Tomography
Waveform inversion
Wavelet transform

PLANETS
Planetary interiors
Planetary volcanism

SEISMOLOGY
Acoustic properties
Body waves
Coda waves
Computational seismology
Controlled source seismology
Crustal imaging
Earthquake dynamics
Earthquake early warning
Earthquake ground motions
Earthquake hazards
Earthquake interaction, forecasting, and prediction
Earthquake monitoring and test-ban treaty verification
Earthquake source observations
Guided waves
Induced seismicity
Interface waves
Palaeoseismology
Rheology and friction of fault zones
Rotational seismology
Seismic anisotropy
Seismic attenuation
Seismic instruments
Seismic interferometry
Seismicity and tectonics
Seismic noise
Seismic tomography
Site effects
Statistical seismology
Surface waves and free oscillations
Theoretical seismology

Tsunami warning
Volcano seismology
Wave propagation
Wave scattering and diffraction

TECTONOPHYSICS
Backarc basin processes
Continental margins: convergent
Continental margins: divergent
Continental margins: transform
Continental neotectonics
Continental tectonics: compressional
Continental tectonics: extensional
Continental tectonics: strike-slip and transform
Cratons
Crustal structure
Diapirism
Dynamics: convection currents, and mantle plumes
Dynamics: gravity and tectonics
Dynamics: seismotectonics
Dynamics and mechanics of faulting
Dynamics of lithosphere and mantle
Folds and folding
Fractures, faults, and high strain deformation zones
Heat generation and transport
Hotspots
Impact phenomena
Intra-plate processes
Kinematics of crustal and mantle deformation
Large igneous provinces
Lithospheric flexure
Mechanics, theory, and modelling
Microstructures
Mid-ocean ridge processes
Neotectonics
Obduction tectonics
Oceanic hotspots and intraplate volcanism
Oceanic plateaus and microcontinents
Oceanic transform and fracture zone processes
Paleoseismology
Planetary tectonics
Rheology: crust and lithosphere
Rheology: mantle
Rheology and friction of fault zones
Sedimentary basin processes
Subduction zone processes
Submarine landslides
Submarine tectonics and volcanism
Tectonics and climatic interactions
Tectonics and landscape evolution
Transform faults
Volcanic arc processes

VOLCANOLOGY
Atmospheric effects (volcano)
Calderas
Effusive volcanism
Eruption mechanisms and flow emplacement
Experimental volcanism
Explosive volcanism
Lava rheology and morphology
Magma chamber processes
Magma genesis and partial melting
Magma migration and fragmentation
Mud volcanism
Physics and chemistry of magma bodies
Physics of magma and magma bodies
Planetary volcanism
Pluton emplacement
Remote sensing of volcanoes
Subaqueous volcanism
Tephrochronology
Volcanic gases
Volcanic hazards and risks
Volcaniclastic deposits
Volcano/climate interactions
Volcano monitoring
Volcano seismology

© 2017 RAS, *GJI*

View publication stats